ACS OMEGA

Morphology-Controlled Tensile Mechanical Characteristics in Graphene Allotropes

Chao Sui,[†,‡,∥] Yushun Zhao,[†,‡,∥] Zhisen Zhang,[†] Jianying He,[*,§] Zhiliang Zhang,[§] Xiaodong He,[‡] Chao Wang,[*,‡] and Jianyang Wu[*,†,§]

[†]Department of Physics, Research Institute for Biomimetics and Soft Matter, Fujian Provincial Key Laboratory for Soft Functional Materials Research, Xiamen University, Xiamen 361005, P. R. China

[‡]Center for Composite Materials and Structures, Harbin Institute of Technology, Harbin 150080, P. R. China

[§]NTNU Nanomechanical Lab, Department of Structural Engineering, Norwegian University of Science and Technology (NTNU), Trondheim N-7491, Norway

S *Supporting Information*

ABSTRACT: A number of graphene allotropes constructed by sp^3, sp^2, and sp hybrid orbitals have recently been proposed to provide the broad potential for practical applications. Here, using molecular dynamics simulation, the structural and tensile characteristics of nine distinct graphene allotropes have been investigated to understand their morphology-controlled mechanical properties. Results show that the averaged out-of-plane displacement is independent of nonhexagons while being dominated by the arrangement of carbon polygons on the sheets. Each sheet possesses unique surface morphology and in-plane tensile properties that significantly vary with morphology and anisotropic crystalline orientation. Brittle, semibrittle, or ductile failure is observed, depending on the

Graphene allotropes Large-scale structural transition

evolution of their packed polygons in facilitating tension deformation and in dissipating energy. Particularly, pentagraphene exhibits superductility as a consequence of large-scale structural transformations, accommodating stress relaxation beyond initial failure. Two distinct plastic deformation patterns in overstretched pentagraphene are uncovered, depending on the tension directions: one is dominated by structural transition from sp^3-carbon-contained penta-(C_5) to mixed sp^2-carbon polygons and the other is mainly controlled by a stepwise pentagon-to-hexagon transition. These findings provide physical insights into the structural evolvement of two-dimensional graphene allotropes and their effects on the mechanical properties.
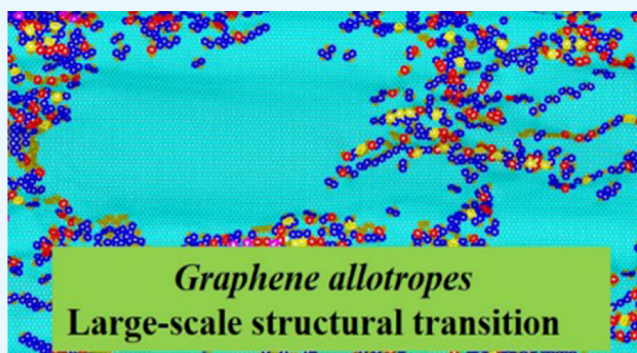
INTRODUCTION

Carbon is one of the unique elements in nature, and it has four electrons in its outermost valence shell for forming sp^n ($n = 1$, 2, 3)-hybridized bonds, yielding a large number of carbon allotropes from zero to three dimensions, such as carbon buckyballs,[1] carbyne,[2] carbon nanotubes (CNTs),[3] graphene,[4] and carbon nanocoils.[5] So far, physical and chemical properties of various carbon allotropes have been experimentally or theoretically identified. For instance, depending on the symmetry of the molecular structure, one-dimensional (1D) carbyne exhibits either metallic or insulating electrical behaviors, and the Peierls transition of carbyne from symmetric sp^2 cumulene to asymmetric sp^1 polyyne structure leads to two distinct electronic properties.[6] The graphene prepared from three-dimensional graphite by using micromechanical cleavage technology,[4] a truly two-dimensional (2D) structure of a carbon allotrope, has been demonstrated to have a number of unique properties, such as the anomalous half-integer quantum Hall effect, the never-falling conductivity, and massless carriers.[7,8] It is believed that carbon sp^2 atoms arranged in a

honeycomb structure of hexagonal polygons are responsible for those extraordinary properties in graphene.

Intrigued by the fantastic properties of 2D graphene mentioned above, the 2D graphene allotropes composed of different topological arrangements of sp^2-carbon atoms have triggered much interest in their unique structures and mechanical properties. Inspired by necessary presence of odd-membered rings (pentagons and heptagons) in helicoidal CNTs[9,10] and spherical fullerenes,[11] Terrones et al.[12] designed three graphene allotropes with different symmetries, named rectangular haeckelite (R-haeckelite), hexagonal haeckelite (H-haeckelite), and oblique haeckelite (O-haeckelite), consisting of ordered arrangements of pentagons, hexagons, and heptagons with sp^2-carbon atoms. All haeckelite structures exhibit an intrinsic metallic behavior independent of orientation. Wang et al.[13] predicted another graphene allotrope with a unit cell of 20
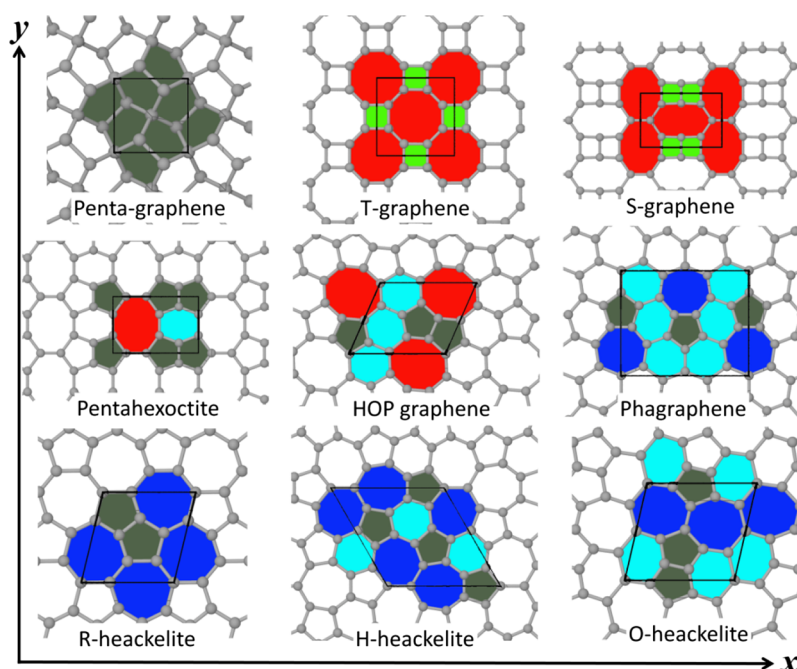
Figure 1. Geometric structures of nine distinct graphene allotropes containing various nonhexagonal carbon rings. Gray balls represent the carbon atoms. Quadrilaterals marked by black solid lines denote a unit cell structure. Color coding for topological polygons, ranging from trigons to decagons, is indicated.

Table 1. Structure and Mechanical Properties of Nine Different Graphene Allotropes

structure	lattice type	polygons per unit cell	atoms per unit cell	hybrid type	tension direction	Young's modulus (N/m)	tensile strength (N/m)	fracture strain (m/m)
pentagraphene	square-like	$4C_5$	6	$sp^3 + sp^2$	x	208.29, 265.0,[18] 376.0,[20] 274.03[21]	27.46, 12.7,[20] 23.51[21]	0.142, 0.051,[20] 0.18[2]
					xy	222.48	24.66	0.108
T-graphene	square-like	$2C_4 + 2C_8$	8	sp^2	x	154.87, 154.45,[22] 168.51,[23] 212[24]	31.52, 27.47,[22] 27.47,[23] 20.2[24]	0.171, 0.238,[22] 0.19[24]
					xy	1979.03, 290.11,[22] 306.86[23]	45.77, 34.17,[22] 34.51[23]	0.033, 0.193[22]
S-graphene	rectangular	$2C_4 + 2C_8$	8	sp^2	x	102.48	18.95	0.103
					y	393.13	34.63	0.160
pentahexoctite	rectangular	$2C_5 + C_6 + C_8$	8	sp^2	x	240.51, 293.0[24]	39.54, 26.9[24]	0.129, 0.2[24]
					y	108.36, 335[24]	40.37, 28.9[24]	0.132, 0.2[24]
HOP graphene	hexagonal	$2C_5 + 2C_6 + C_8$	10	sp^2	x	243.69	44.95	0.124
					y	231.34	34.42	0.131
phagraphene	rectangular	$2C_5 + 6C_6 + 2C_7$	20	sp^2	x	433.42, 275.71[21]	46.09, 25.39[21]	0.449, 0.18[21]
					y	295.96, 274.03[21]	48.32, 25.57[21]	0.146, 0.16[21]
R-haeckelite	hexagonal	$2C_5 + 2C_7$	8	sp^2	x	329.54	34.33	0.203
					y	332.93	35.89	0.136
H-haeckelite	hexagonal	$3C_5 + 2C_6 + 3C_7$	16	sp^2	x	315.64	33.12	0.124
					y	459.96	35.73	0.156
O-haeckelite	hexagonal	$2C_5 + 2C_6 + 2C_7$	12	sp^2	x	233.28	32.28	0.128
					y	307.26	43.37	0.277

sp^2-carbon atoms, termed phagraphene, which is also composed of pentagons, hexagons, and heptagons. It was found that phagraphene possesses distorted Dirac cones and the direction-dependent cones are robust against an external strain with tunable Fermi velocities. On the other hand, several 2D carbon sheets made of pentagons, hexagons, and octagons, such as pentahexoctite and HOP graphene, were found.[14,15] Similarly, the pentahexoctite and HOP graphene both present metallic behaviors. In addition to those graphene allotropes containing odd-membered rings, other two carbon allotropes called T-graphene and S-graphene containing only tetrarings and

octarings were proposed.[16,17] T-graphene can be planar or buckled, depending on the number of square sublattices in a unit cell and planarity of two adjacent square sublattices. In contrast to planar T-graphene, buckled T-graphene has Dirac-like fermions with a high Fermi velocity. Recently, a novel 2D structure of graphene allotrope exfoliated from T12-carbon was proposed and named pentagraphene by Zhang et al.[18] Unlike the above graphene allotropes, pentagraphene consisting of only pentagons is a mixed sp^2–sp^3-hybridized system of carbon with one-third of sp^3-carbon atoms and two-third of sp^2-carbon atoms. It is corrugated in out-of-plane direction in a periodic
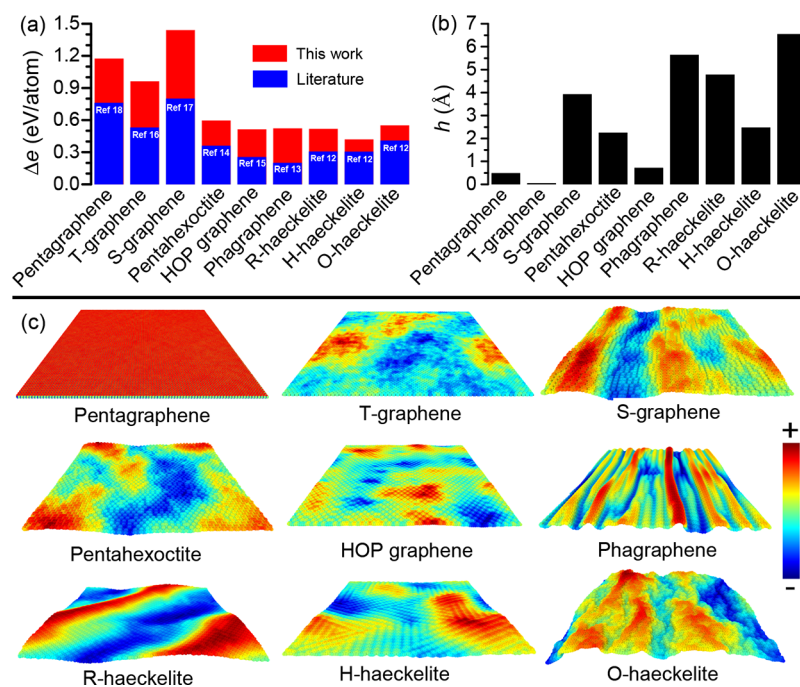
Figure 2. (a) Difference in the potential energies between nine graphene allotropes and graphene from our MD calculations and available data of first-principles calculations in the literature. (b) Averaged out-of-plane displacement amplitude of nine graphene allotropes. (c) Diverging out-of-plane displacement field of nine graphene allotropes. The red and blue colors of atom represent positive and negative atomic displacements along the out-of-plane z direction, respectively.

manner because of the tetrahedral character of the sp^3-hybridized bonds.

Because of their ultrathin 2D nature, these graphene allotropes possess unique mechanical properties and hence possess unique electrical properties.[16,18] Therefore, fundamental studies on the relationships between their structures and mechanical properties are necessary to guide their applications. Although some efforts have been made to understand their mechanical properties,[18−26] they are still limited, particularly in anisotropic deformation responses, strain-induced structural transition, and fracture mechanisms. Therefore, this study aims to explore the mechanical characteristics of nine distinct graphene allotropes containing nonhexagonal carbon rings under uniaxial tension by large-scale molecular dynamics (MD) simulations, thus providing physical insights into the tensile properties of graphene allotropes with different topological arrangements of carbon polygons.

■ RESULTS AND DISCUSSION

Surface Morphology. Nine distinct graphene allotropes including pentagraphene, T-graphene, S-graphene, pentahexoctite, HOP graphene, phagraphene, R-haeckelite, H-haeckelite, and O-haeckelite, with topological carbon polygons from tetragon to octagon, are taken into investigation. Top views of atomistic lattices of these carbon nanostructures along with unit cells are presented in Figure 1. More detailed structural information about the nanostructures is listed in Table 1. All studied monolayer sheets are generated to be approximately 300×300 Å^2 in dimensions during the MD simulations. The number of carbon atoms varies from 30 720 to 46 464, depending on the type of graphene allotropes.

To evaluate the comparative stability of these graphene allotropes, the total potential energies are calculated from the relaxed structures at 10 K. The MD simulation differs from the predictions at the ground energy state by first-principles calculation, in which a small number of atoms are employed and out-of-plane atomic displacements usually do not occur after relaxation. The differences in the energies per atom (Δe) between the examined allotropes and pristine graphene are calculated as follows

$$\Delta e = E_{\text{tot(sheet)}}N - e_0 \tag{1}$$

where $E_{\text{tot(sheet)}}$ is the total potential energy of relaxed graphene allotrope sheets of N atoms and e_0 is the energy per atom in a perfect graphene sheet. It can be seen from Figure 2a that potential energies of all examined graphene allotropes relative to those of pristine graphene are positive, implying that they are metastable. It suggests that the formation of graphene allotropes composed of tetrarings will be most energy-unfavorable. The most stable structures are allotropes constructed by periodically distributed C_n carbon rings, where $n = 5$, 6, 7, and 8. Particularly, the pentagraphene made of purely pentagonal rings is excluded because of its violation of isolated pentagon rules and mixed sp^2–sp^3-hybridized bonds. It is noted that some carbon allotropes with high energies, such as C_{20} fullerene,[27] carbyne,[6,28] and graphene containing high concentrations of C_4–C_8 rings,[29] have been successfully synthesized in laboratory settings, which implies that they could be thermodynamically metastable.

At nonzero temperature, thermal-induced out-of-plane fluctuations with ripples spontaneously appear in a 2D lattice and distort the lattice. The characteristic length of the ripples falls in the range of the averaged out-of-plane displacement, which is defined as

$$\langle h \rangle = \sqrt{\sum_{i}^{N} m_i (h_i - h_{\text{com}})^2 / \sum_{i}^{N} m_i} \tag{2}$$
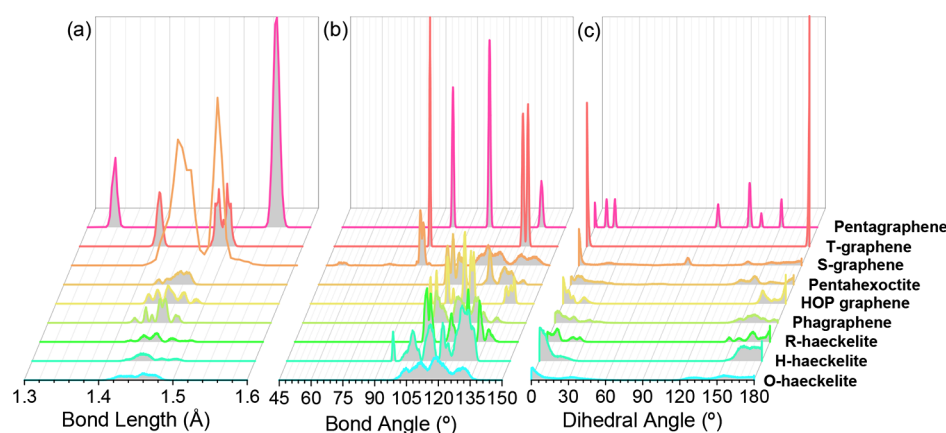
Figure 3. Comparison of distribution profiles of (a) bond length, (b) bond angle, and (c) dihedral angle for the nine relaxed graphene allotropes. Distinct structural parameters in these graphene allotropes are indicated.

where h_{com} is the position in the normal (z) direction of the examined whole graphene allotrope sheet and m_i and h_i are the mass and the position in the normal (z) direction of the i atom, respectively. The calculated value of averaged out-of-plane displacement for relaxed graphene allotropes at 10 K is presented in Figure 2b. Distinct averaged out-of-plane displacements varying from around 0.048 to 6.549 Å are observed, suggesting a strong structure-dependent thermal-induced out-of-plane displacement. These averaged out-of-plane displacements are substantially larger than the magnitude of intrinsic ripples in the pristine graphene sheet under the same conditions. It can be found that the relationship of averaged out-of-plane displacements for graphene allotropes is on the order of $\langle h \rangle_{\text{T-graphene}} < \langle h \rangle_{\text{pentagraphene}} < \langle h \rangle_{\text{HOP graphene}} < \langle h \rangle_{\text{pentahexoctite}} < \langle h \rangle_{\text{H-haeckelite}} < \langle h \rangle_{\text{S-graphene}} < \langle h \rangle_{\text{R-haeckelite}} < \langle h \rangle_{\text{R-haeckelite}} < \langle h \rangle_{\text{phagraphene}} < \langle h \rangle_{\text{O-haeckelite}}$. T-graphene, pentagraphene, and HOP graphene yield $\langle h \rangle$ of 1.0 Å, comparable to the interatomic C−C distance. For T-graphene, the averaged out-of-plane displacement of 0.048 Å confirms that its geometry is planar, which is in agreement with the judgment from quantum MD simulations.[30] It is noted that pentagraphene has an intrinsic out-of-plane buckling distance of 0.48 Å in our simulation. By excluding the effect of intrinsic buckling, pentagraphene has the smallest thermal rippling amplitude (around 0.001 Å). This small height fluctuation is induced by the fact that in pentagraphene, the in-plane bending modes, that is, modes involving C−C−C bond angles in the buckled structure, can accommodate the thermal energy, which is the same as that in suspended graphene.[31] Distinct out-of-plane displacements in T-graphene and S-graphene with identical tetragons and octagons are present in their unit cells, which indicates that there is no clear correlation between the averaged out-of-plane displacement and nonhexagons on the carbon sheets. Furthermore, other structures containing heptagons and heptagons and octagons also demonstrate that the percentage of nonhexagons in graphene allotropes is not closely relative to the averaged out-of-plane displacement. Instead, the averaged out-of-plane displacement is mainly determined by the arrangement of carbon polygons on the sheets. In graphene, few nonhexagons lead to remarkable out-of-plane deformations, while the out-of-plane wrinkle pattern can be completely suppressed once the number of nonhexagons reaches to a critical value.[32]

To illustrate the difference in averaged out-of-plane displacement of these sheets in depth, their relaxed morphologies,

where the carbon atoms are colored according to their positions in the normal (z) direction, are captured and are shown in Figure 2c. Distinct structural morphologies of these relaxed sheets are observed. Both pentagraphene and T-graphene show a larger wavelength pattern but smaller local curvatures. These small local curvatures are profited from nondistorted lattices, which can explain their small averaged out-of-plane displacements. However, all other structures present not only significant out-of-plane fluctuation but also large local curvatures, confirming their relatively larger averaged out-of-plane displacement. The configurations of T-graphene and S-graphene imply that the arrangement of nonhexagons dominates the global and local structural morphologies. Interestingly, the out-of-plane fluctuation of phagraphene and R-haeckelite sheets features 1D wavy patterns instead of 2D checkerboards observed in other sheets. The short-wavelength pattern along the y direction in phagraphene mainly results from the row of dense topological structure of pentagon−heptagon pairs. However, in the case of R-haeckelite, a significant long-wavelength pattern is found. Moreover, regularly small wavelike ripples, that is, well-arranged local wrinkles caused by the specific arrangement of nonhexagons, are also observed on the thermal-induced curved surface of H-haeckelite, R-haeckelite, and HOP graphene sheets, in contrast to those in S-graphene and O-haeckelite. Overall, the physical origin of the observed fluctuations in these graphene allotropes containing dense nonhexagons originates from the coupling of the out-of-plane displacement with the in-plane strain.

Bond Characteristics. Figure 3 shows the distribution profiles of bond lengths, bond angles, and dihedral angles of relaxed graphene allotropes at a low temperature of 10 K. Unlike graphene, a wide distribution of bond lengths, bond angles, and dihedral angles and a number of peaks in the curves are observed. For pentagraphene, the distribution of bond lengths shows two peaks at around 1.338 and 1.555 Å, corresponding to the sp^2 and sp^3 bonds, respectively. This is in good agreement with that of previous ab initio calculations by Zhang et al.[18] Three peaks at around 97°, 115°, and 139° correspond to bond angles of $\theta_{C(sp^2)-C(sp^3)-C(sp^2)}$ connecting four pentagons, $\theta_{C(sp^3)-C(sp^2)-C(sp^2/sp^3)}$ in pentagons, and $\theta_{C(sp^2)-C(sp^3)-C(sp^2)}$ in pentagons in relaxed pentagraphene, respectively. Strikingly, different bond angles deviating from 109.471° of diamond in tetrahedral structures show the distorted $C_{(sp^3)}$ character, which is consistent with the previous report by Zhang et al.[18] As indicated by the peaks in the
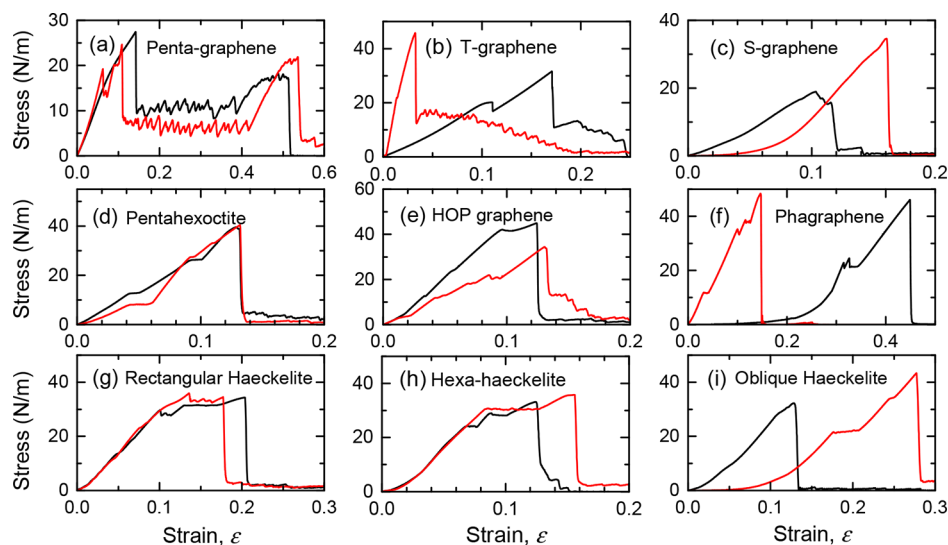
Figure 4. Tensile mechanical stress−strain diagrams of (a) pentagraphene and (b) T-graphene subjected to uniaxial deformation along the x and xy directions, respectively, as well as (c) S-graphene, (d) pentahexocite, (e) HOP graphene, (f) phagraphene, (g) R-haeckelite, (h) H-haeckelite, and (i) O-haeckelite subjected to uniaxial tensile loads along the x and y directions at a low temperature of 10 K.

distribution of dihedral angles in Figure 3c, there also exist different types of dihedral angles, which are approximately 0°, 9°, and 16° in pentagons and 99°, 125°, 134°, and 151° connecting pentagons. These dihedral angles correspond to $\theta_{C(sp^3)-C(sp^2)-C(sp^2)-C(sp^3)}$, $\theta_{C(sp^2)-C(sp^2)-C(sp^3)-C(sp^2)}$ #1, and $\theta_{C(sp^2)-C(sp^2)-C(sp^3)-C(sp^2)}$ #2 in pentagons and $\theta_{C(sp^2)-C(sp^2)-C(sp^3)-C(sp^2)}$ #1, $\theta_{C(sp^2)-C(sp^2)-C(sp^3)-C(sp^2)}$, $\theta_{C(sp^3)-C(sp^2)-C(sp^2)-C(sp^3)}$, and $\theta_{C(sp^2)-C(sp^2)-C(sp^3)-C(sp^2)}$ #2 connecting pentagons. Different dihedral angles in pentagons suggest that pentagons in pentagraphene are nonplanar. By inspecting the cases of T-graphene and S-graphene made of tetragons and octagons, distinct distributions of bond length, bond angle, and dihedral angle are observed, indicating multiplicity of carbon. Three types of bonds, which are about 1.41 Å for octagons and 1.49 and 1.50 Å shared by tetragons and octagons, respectively, exist in T-graphene, whereas some types of bonds are in S-graphene because of broad distribution of bond lengths. Similarly, three types of bond angles, which are around 90° in tetragons and 134° and 136° in octagons, are observed in T-graphene. Two sharp peaks at 0° and 180° found in the distribution of dihedral angles of T-graphene indicate its locally planar surface structure. Whereas broad distribution of dihedral angles of S-graphene implies its locally wrinkled morphology, confirming the results presented in Figure 2c. However, for other sheets including pentagons and heptagons, complicated distributions of bond length, bond angle, and dihedral angle were observed in Figure 3. In short, bond lengths and bond angles of all graphene allotropes deviating from 1.42 Å and 120° of graphene suggest that an intrinsic strain is introduced in their internal structures, resulting in a decrease in the stability relative to graphene. Additionally, dihedral angles deviating from 0° or 180° explain the out-of-plane atomic displacements.

Tensile Mechanical Properties. In this subsection, the tensile mechanical characteristics of these 2D sheets are investigated. Figure 4 shows their stress−strain relationships under uniaxial tensile loading along the x and y directions at a low temperature of 10 K. Apparently, all graphene allotropes exhibit strongly distinct nonlinear behaviors, and three or four

different deformation regimes can be identified, depending on the structures of graphene allotropes and tensile directions.

In the first regime, tensile stiffness in S-graphene, phagraphene, R-haeckelite, H-haeckelite, and O-haeckelite structures increases with an increasing strain, similar to the characteristics of entropic elastic responses of thin membranes. The wrinkles with large out-of-plane displacements as a result of the presence of nonhexagonal rings and thermal fluctuations are responsible for the entropic elasticity. This behavior is also found in polycrystalline graphene.[33] Furthermore, as shown in Figure 4c,f,i, the stress−strain relationships of S-graphene, phagraphene, and O-haeckelite demonstrate strong chirality-dependent tensile stiffness. Feature of 1D wave-formed ripples in these relaxed structures is mainly attributed to initially different mechanical responses; stretching of the structures along the ripple direction leads to high tensile stiffness, whereas low tensile stiffness is observed when they are strained perpendicular to the ripple direction. Graphene allotropes with small out-of-plane fluctuations, including pentagraphene, T-graphene, pentahexocite, and HOP graphene, are observed to follow almost initially linear stress−strain responses. Therefore, nanoscale dewrinkling is the main deformation mechanism in the first regime. In the second regime, as the strain increases, the tensile stress nonlinearly increases up to a maximum value, referred to as maximum tensile strength. The wrinkles in the sheets are largely flattened by the applied deformation in this phase. The C−C bonds nonparallel to the stretching direction are directly stretched, whereas those perpendicular to the tensile direction are contracted. Particularly, abrupt drops or plateau of tensile stress occurring in the loading curves implies the occurrence of structural transformations in the sheets caused by excessive deformation. No plastic deformation occurs during this straining process. In the third regime, a deepest drop of tensile stress in the stress−strain curves occurs, except in the case of pentagraphene. Such a reduction in tensile stress indicates the failure of the sheets due to fracture. The fourth deformation regime exclusively points at pentagraphene and T-graphene. It is observed from Figure 4 that, among others, pentagraphene and T-graphene exhibit apparent features of ductile characteristics in the loading
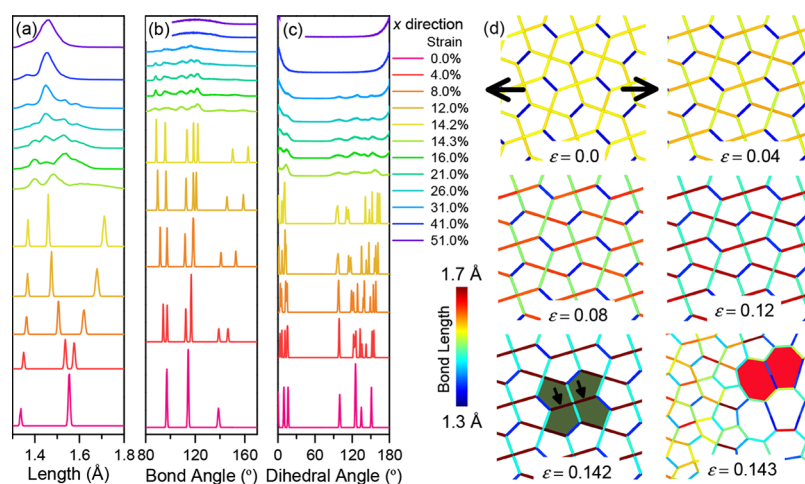
Figure 5. Distribution profiles of (a) bond length, (b) bond angle, and (c) dihedral angle as a function of strain as well as (d) development of representatively zoomed-in structural motifs of pentagraphene when uniaxial tension is applied on pentagraphene along the x direction. Two arrows in the left-top snapshot indicate the straining direction on pentagraphene. Colored polygons in bottom snapshots explain the structural transition from pentagons to octagons as a result of dissociation of two C−C bonds (marked by two arrows). C−C bonds are colored according to their bond length.
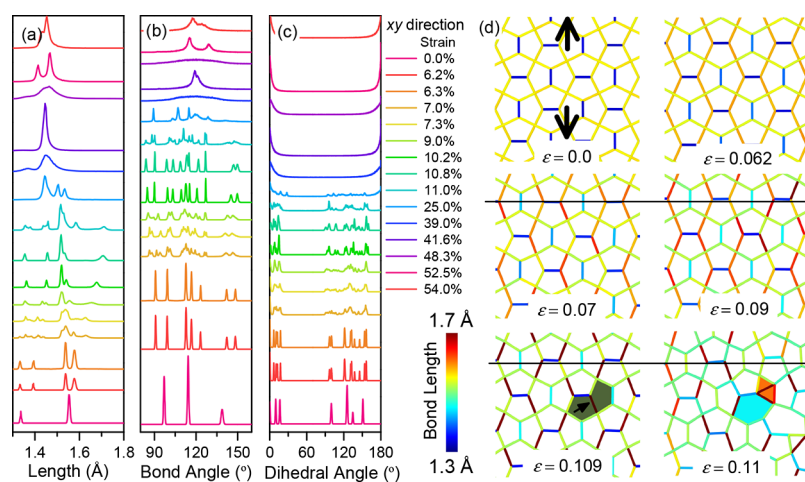

Figure 6. Distribution profiles of (a) bond length, (b) bond angle, and (c) dihedral angle as a function of strain when uniaxial tension is applied on pentagraphene along the xy direction as well as (d) representatively zoomed-in structural motifs of pentagraphene at several critical strains. Two arrows in the zoomed-in structure with zero strain indicate the tension direction applied on pentagraphene. One C−C bond in the zoomed-in structure with a strain of 0.09 can be identified to be nonparallel to the horizontal solid line, implying the appearance of nonuniformly local strain for 2 equiv bonds of pentagons. One arrow in the left-bottom snapshot points out the dissociation of one C−C bond due to excessive local strain. Specifically, neighboring polygons dyed by colors in bottom snapshots clearly illustrate the transition of pentagon to hexagon in overstretched pentagraphene. C−C bonds are colored according to their bond length.

curves for both tension directions. Interestingly, differing from other sheets, pentagraphene can still endure large strain after fracture at a strain of around 0.12, and the load stress does not decline but oscillates between values of 5−8 and 8−11 N/m under the x and y tensile directions, respectively. This suggests that the structure undergoes a series of repeating process of local strain and local stress relaxation, exhibiting superplastic deformation behavior. Moreover, prior to the deepest drop of tensile stress at a large strain of around 0.5, a steep increase in tensile stress appears in the loading curves of pentagraphene as the applied strain is augmented, which is indicative of stretching a stable as-formed structure.

Mechanical parameters such as Young's modulus, ultimate tensile strengths, and fracture strains as well as available data from the literature[18,20−24] are shown in Table 1 for comparison. Effective Young's modulus is determined by fitting the linear

regime of the stress−strain curves, instead of the initial elasticity caused by the entropic effect. Although there is some scatter in the previously reported results by density functional theory (DFT), the results by Reax forcefield (ReaxFF) MD calculations in this study are almost consistent with them, except for T-graphene under xy-uniaxial tension. As can be seen in Table 1, all investigated sheets show desirable tensile properties in terms of in-plane stiffness and tensile strength. Moreover, anisotropic tensile properties in these 2D sheets can be identified, mainly attributed to their topological structures. These sheets can be sorted in terms of x-directional tension in-plane stiffness from the highest to the lowest values of Young's modulus as phagraphene > R-haeckelite > H-haeckelite > HOP graphene > pentahexoctite > O-haeckelite > pentagraphene > T-graphene > S-graphene, whereas for y/xy-directional tension, they can be sorted as T-graphene > H-haeckelite > S-graphene
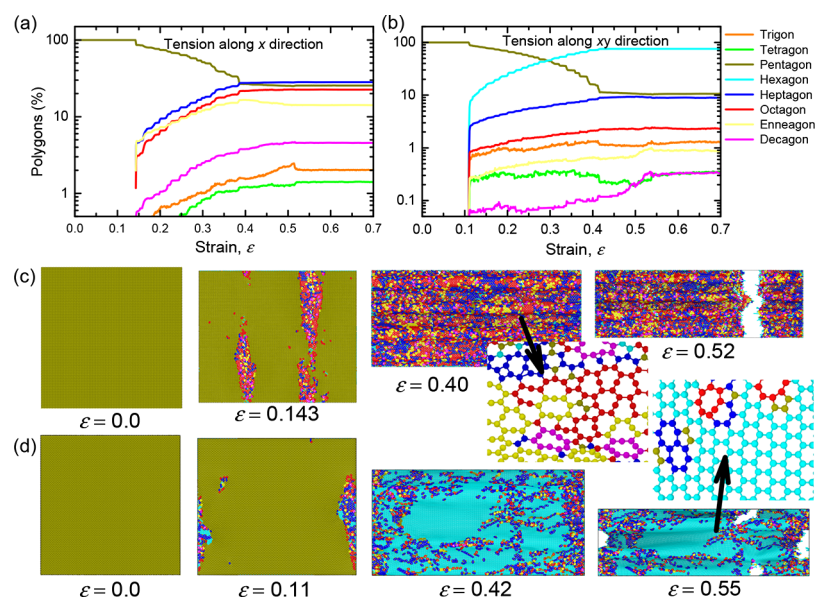
Figure 7. Strain-induced large-scale structural transformations in pentagraphene. Variation in the percentages of C_3–C_{10} polygons to overall carbon polygons in pentagraphene with the applied uniaxial strain along (a) x and (b) xy directions. Tension-dependent large-scale structural transformations in pentagraphene are attributed to a significant difference in the ratios of each polygon to all polygons. Intermediate heterostructures composed of frustrated and intact pentagraphene form during the structural transformation. Formation of hexagons during the deformation is limited by the angular constraint of simulation box to some extent. Typical snapshots of pentagraphene at critical strains when uniaxial tension is applied along (c) x and (d) xy directions. Two typical microstructures in the fully fractured pentagraphene are intentionally captured to distinguish structural transitions caused by straining along the x and xy directions. Carbon atoms are dyed according to one type of topologically polygonal ring constructed by them, in line with those of the corresponding curves.

> R-haeckelite > O-haeckelite > phagraphene > HOP graphene > pentagraphene > pentahexoctite. In terms of x-directional tensile strength from the highest to the lowest values, they are sorted as phagraphene > HOP graphene > pentahexoctite > R-haeckelite > H-haeckelite > O-haeckelite > T-graphene > pentagraphene > S-graphene, whereas in the case of y/xy direction, they can be sorted as phagraphene > T-graphene > O-haeckelite > pentahexoctite > R-haeckelite > H-haeckelite > S-graphene > HOP graphene > pentagraphene. The large fracture strain observed in phagraphene and O-haeckelite is due to their highly wrinkled morphology.

These findings indicate that an atomically structural morphology dominates the mechanical properties of graphene allotropes, although previous studies suggested that mechanical and physical properties of 2D nanomaterials can be finely tuned by surface chemical functionalization.[34,35]

Effect of Structures on Tensile Mechanical Behaviors. Structural parameters such as bond lengths, bond angles, and dihedral angles are the three important factors that control the deformation of these 2D materials. Figures 3, 5, and S1–S8 (see Supporting Information) show the distribution profiles of bond lengths, bond angles, and dihedral angles at different tensile strains for the graphene allotropes subjected to two different uniaxial directions. For all structures, as the applied strain is augmented in the elastic regime, specific peak in the curves of distribution of bond lengths and bond angles splits up into two or more sharp peaks, and changes in the position of the peaks simultaneously happen. When the tensile strain exceeds a critical value, a change in both the number and the position of the peaks occurs, and sharpness of the peaks decreases. To give a more clear picture of the bond and bond angle deformation, typically local snapshots of pentagraphene at several critical strains under both x- and xy-uniaxial elongations are, respectively, captured, as shown in Figures 5d and 6d. As

presented in Figure 5d, elastic elongation of pentagraphene along the x direction leads to distinct variations in the length of 4 equiv C–C bonds in a pentagon; two bonds that are placed to be small angles to the tension direction are stretched; however, the other two ones that make large angles along the straining direction are contracted. This explains the decomposition of one peak at 1.555 Å presented in Figure 5a. Contrarily, length in unique bond constructed by sp^2 carbons in pentagons monotonically increases with an increase in the strain. Similarly, in the case of xy-uniaxial direction, atomic bonds in pentagons, which make small angles or are parallel to the stretching direction, have a significant contribution to the applied strain. Intriguingly, as the sheet is deformed beyond a strain of 0.09, the bonds originally perpendicular to the tension direction realign. This deformation mechanism results in a sudden bond transformation of the adjacent bonds. Such a bond realignment confirmed by horizontal solid lines across the snapshots in Figure 6d explains the first drop in load stress, as observed in Figure 4a, as well as the distinct changes in the distribution profiles of bond lengths presented in Figure 6a.

In addition to bond stretching and contraction, great angular and torsional deformations indicated by Figures 5b,c and 6b,c, where significant deviations of the characteristic bond angles and dihedral angles relative to the initial states are observed, also help accommodating the applied tensile strain. These microstructural changes can also be confirmed by the analysis of local atomic shear strains (Figure S9 in Supporting Information). The maximum ratio of bond stretch to bond angle bending for all sheets under elastic deformation is plotted in Figure S10 in the Supporting Information. From Figure S10, it is revealed that the interplay among bond stretch, bond angle bending, and lattice orientation determines the tensile properties such as in-plane stiffness, tensile strength, and fracture strain. For example, although pentagraphene has identical
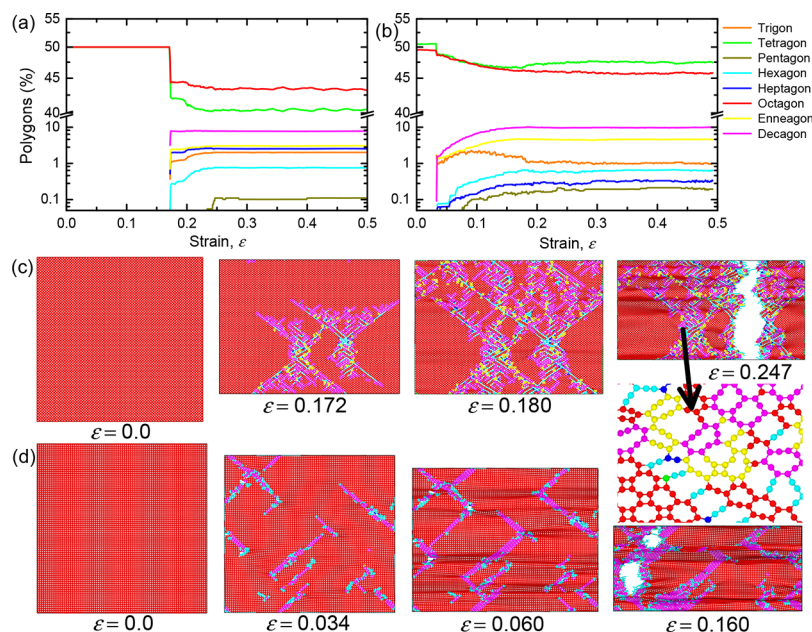
Figure 8. Structural transformations in T-graphene driven by tension. Percentage of C_3–C_{10} polygons to overall carbon polygons identified in T-graphene as a function of strain when uniaxial tension is imposed on T-graphene along (a) x and (b) xy directions. Typical snapshots of T-graphene are captured at several critical strains when uniaxial tension is applied along (c) x and (d) xy directions. One typical microstructure in the bulk pentagraphene is zoomed-in to clearly show the structural transformation due to bond dissociation. No difference in the structural transformations between both stretching directions is detected. Carbon atoms are painted according to one type of topologically polygonal ring constructed by them, in line with those of the corresponding curves.

values of maximum ratio of bond stretch (from 1.555 to 1.711 Å) under exposure to the two directional elongations, larger maximum ratio of bond angle bending under x-directional tension produces higher tensile strength and fracture strain. Furthermore, significant difference in the structural load distributions for the two uniaxial tensions demonstrates disparate failure modes. For the x-directional tension, excessive external load causes dissociation of one of the highly stretched bonds in pentagons, yielding sp^2-carbon octagons in which one atom is connected by only two atoms, as illustrated by color-filled polygons in Figure 5d. Such a production of octagons is also accompanied by a rapid structural transition of sp^2/sp^3-carbon pentagons to other sp^2-carbon polygons. These structural transformations are also greatly hinted by huge changes in the distribution profiles of bond, bond angle, and dihedral angles. For the xy-directional tension, the highly stretched bond in pentagons is broken in the same manner as the applied load stress exceeds the strength of $C_{(sp^2)}$–$C_{(sp^3)}$ bond. Such a bond dissociation, however, does not lead to the formation of an octagon. Instead, two new bonds form between two pentagons shared by the dissociated bond, resulting in a structural transition from two adjacent pentagons to a hexagon plus two trigons, as shown in the bottom snapshots of Figure 6d. Likewise, distribution profiles of bond, bond angles, and dihedral angles dramatically change, as shown in Figure 6a−c. More interestingly, when elongation is further applied, two intact bonds on the two metastable trigons immediately dissociate, yielding two newly adjacent hexagons. Ideally, perfect graphene can be acquired from pentagraphene by the stepwise xy-directional strain-triggered structural transformations, which are consistent with the energy-favorable route proposed by Ewels et al.[36] Notably, classic MD simulation in this study demonstrates a clear dynamic process of the

structural transformations, contrasting with the prediction by static DFT calculations at the ground state.[36]

To provide more insights into the changes in polygonal topologies during structural transformations in the pentagraphene, ring statistics of the polygons with a size ranging from trigons to decagons in sheets with the applied strain is analyzed. Figure 7 compares relationships between percentages of C_3–C_{10} polygons to overall carbon polygons in the pentagraphene and tensile strain along the x and xy directions, respectively, as well as their typical snapshots at critical strains. Clearly, within the elastic limit, pentagons dominate the ring statistics along both tension directions, as shown in Figure 7a,b. Beyond the elastic limits, the ratio of hexagon to all polygons reduces in a stepwise manner as strain increases up to around 0.4. Inversely, the stepwise increase in the ratio of other types of polygons to all polygons occurs in the deformation phase, quantitatively describing the dissociation of sp^3-carbon-contained pentagons accompanied by the formation of various sp^2-carbon polygons. Such stepwise changes in percentages of various polygons correspond to the oscillations of load stress in the curves shown in Figure 4a. As the applied strain exceeds 0.4, the ratios of each type of polygon to all polygons remain nearly constant, indicating the accomplishment of structural transformations. However, significantly quantitative discrepancies in the ratios of each polygon to all polygons in completely frustrated pentagraphene along the x and xy directions reveal strikingly distinct scenarios of structural transformations, as hinted by bottom snapshots in Figures 5d and 6d. For the x-directional tension, the completely frustrated pentagraphene is composed of sp^2-carbon pentagons (25.5%), hexagons (28.2%), heptagons (22.5%), and octagons (14.2%), whereas for the xy-directional stretch, only the hexagon (approximately 76%) mainly dominates the polygon statistics, as visually demonstrated in Figure 7c,d. Such a distinct disparity is attributed to markedly
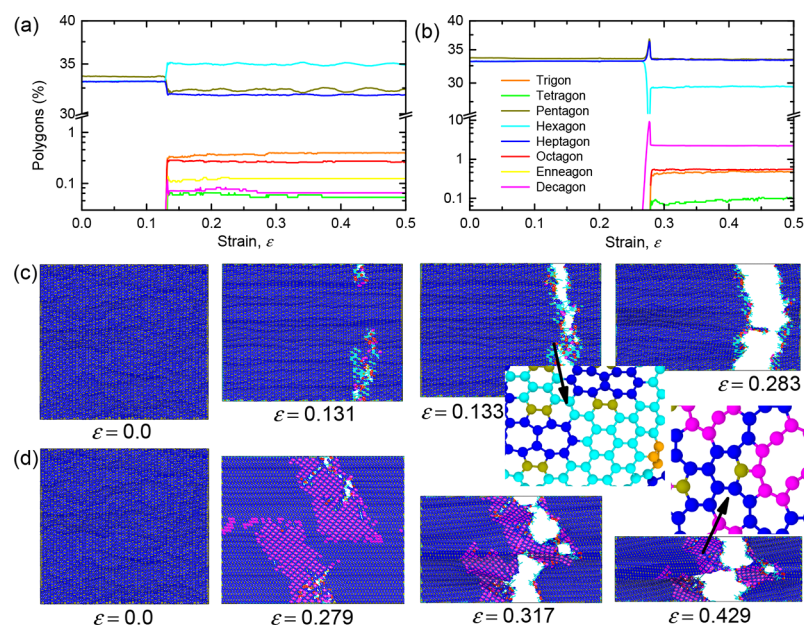
Figure 9. Structural transformations in O-haeckelite triggered by straining. Relationships between percentages of C_3-C_{10} polygons to overall carbon polygons in O-haeckelite and strain when it is subjected to uniaxial deformation along (a) x and (b) y directions, respectively. Typical snapshots of O-haeckelite when uniaxial tensile strain is forced along (c) x and (d) y directions, respectively. Two local microstructures of pentagraphene are captured to reveal the structural transitions. Limited hexagons close to the cracking edges form due to bond rotations for x-directional tension, whereas for the y-directional tension, numbers of decagons appear as a result of bond dissociations that are shared by pentagons. Carbon atoms are colored according to one type of topologically polygonal ring constructed by them, in line with those of the corresponding curves.

different scenarios in the distribution of atomic stress on frustrated and intact zones of pentagraphene. The atoms located at just frustrated zone have higher von Mises stress than those at intact one along the x direction; however, high atomic von Mises stress is concentrated on intact pentagraphene along the xy direction, as shown in Figure S11 in the Supporting Information. As a result, steep stress gradient occurs at the mismatched heterointerfaces, as clearly illustrated by the zoomed-in snapshots in Figure S11, which enhances the strain-induced structural transitions in pentagraphene. This is also indicated by the magnitude of the averaged load stress in the curves shown in Figure 4a, where larger oscillations of load stress are observed for the x-directional tension than those observed for the xy-directional tension. Additionally, the hexagon-dominated structure explains an observation of large load stress at the end of elongation for the xy-directional tension. Heterointerfaces between intact and frustrated pentagraphene are locally wrinkled because of the difference in their planarity. Interestingly, different width in the in-plane transverse direction perpendicular to tension direction between intact and frustrated pentagraphene causes the in-plane transverse tensile/compressive stress as a result of the intrinsic difference in their planar atomic densities. As shown in Figure S12, for the x-directional tension, small height of ripples in frustrated pentagraphene suggests that it is biaxially stretched, in contrast with that for the xy-directional strain. This again indicates the tension direction dependence of large-scale structural transformations in pentagraphene.

For comparison, analysis of polygon statistics in other carbon sheets as a function of the applied strain is also performed, as presented in Figures 8a,b, 9a,b, and S13−S18 in the Supporting Information. All curves show a sharp change in the percentages of C_3-C_{10} polygon to overall polygons, implying their initial failures caused by stretch. Posterior to the sudden change in

ring statistics, the number of polygons, including the newly formed ones, levels off soon. It is also evident that the change in the ratios of the dominated polygons to overall polygons on these carbon sheets is significantly smaller than that on pentagraphene. These suggest a lower tensile ductility than that of pentagraphene. Intriguingly, pentahexoctite, HOP graphene, phagraphene, and O-haeckelite show an apparent increase in the ratio of one originally dominated polygon to all polygons beyond the initial fracture strain for one specific tension direction, indicating direction-dependent failure mechanisms. To reveal the failure mechanisms of these carbon sheets, several snapshots of graphene allotropes excluding pentagraphene subjected to two different directional strains are captured and are shown in Figures 8c,d, 9c,d, and S19−S26. On the basis of the patterns of fracture edges, it is found that S-graphene shows brittle failures (straight crack) for both tension directions, whereas phagraphene can show either brittle or semibrittle fracture, depending on the tension direction, and pentahexoctite, HOP graphene, phagraphene, R-haeckelite, and H-haeckelite demonstrate direction-independent semibrittle failures. Notably, T-graphene shows ductile failure for both tension directions, as illustrated by Figure 9c,d, where large numbers of decagons (around 10%) via breakage of bonds shared by tetra- and octagons form in T-graphene for both tension directions prior to deadly fracture. In particular, O-haeckelite, with an exception, shows either brittle or ductile plastic deformations, depending on the tension directions. For the x-directional tension, structural transition from quite limited Stone−Thrower−Wales (or 5775) defects to crystalline structures with hexagonal (6666) topology (<2%) via bond rotation opens cracks to complete fracture (Figure 9c), whereas for the y-directional stretch, a decagonal structure forms over a large area in T-graphene because of dissociation of bonds shared by adjacent pentagons in facilitating excessive

deformation (Figure 9d). It can be concluded that failure patterns in graphene allotropes are strongly sensitive to their structural morphologies and tension directions.

CONCLUSIONS

In this work, we have quantified the structural and in-plane mechanical properties of nine different graphene allotropes by using large-scale MD simulations. The calculation results show that the investigated structures possess higher energies than the indefective graphene. The sp^2-carbon penta-, hexa-, hepta-, and octagon-contained sheets are energetically comparable. However, great differences are identified in the surface morphology of all relaxed structures and in the tension direction-dependent stress–strain responses that resulted from the arrangement of carbon polygons. Significant differences are also observed in maximum bond length prior to initial failures and in the characteristic bond angles and dihedral angles relative to the initial states, indicating that angular and torsional deformations also help accommodating the applied tensile strain. Brittle, semibrittle, and ductile failure patterns are detected in these 2D structures, and two different failure patterns are observed in S-graphene and O-haeckelite. Failures occurring in overstretched sheets are associated with the evolution of packed non-hexagons. Specifically, pentagraphene exhibits extraordinary stretchability under two different tension directions, and the high ductility is attributed to two distinct large-scale structural transitions. This work provides a fundamental understanding on tensile mechanical characteristics and their relationship with the structural evolvement of planar carbon nanostructures.

MODELS AND METHODOLOGY

All classic MD simulations are carried out by using the large-scale atomic-molecular massively parallel simulator code package.[37] The carbon–carbon atomic interactions in the graphene allotrope systems are described by the first-principles-based ReaxFF potential in the MD simulations. The ReaxFF is capable of capturing all possible interactions including covalent terms, Coulomb interactions, dispersion, and other nonbonding forces. It is also able to handle chemical reactions, including chemical bond formation and breaking according to bond order values. Previous studies showed that ReaxFF accurately predicts the mechanical behaviors of hydrocarbons, CNTs, graphite, diamond, and other carbon-based nanostructures.[38] The version of the ReaxFF developed by Chenoweth et al.[39] is employed in this study. It is noted that this potential can well-reproduce intrinsic buckling characteristics of pentagraphene, contradicting that a flat pentagraphene was described by the reactive empirical bond order potential.[40] The buckling distance in the out-of-plane direction of pentagraphene is determined to be about 0.48 Å, which agrees with that calculated by ab initio calculations.[18]

Prior to the uniaxial loading, all isolated graphene-allotropes are first quasistatically relaxed to a local minimum energy configuration via the conjugate gradient method with an energy tolerance of 1.0×10^{-4} eV and a force tolerance of 1.0×10^{-4} eV/Å. A small timestep of 0.1 fs with the velocity-Verlet integration algorithm is utilized, making sure that the MD simulation process is stable. Periodic boundary conditions are applied in planar directions to simulate an infinite sheet, which eliminates any spurious effects of boundaries during tension. MD relaxations of 50 ps (500 000 timesteps) are carried out at zero pressure in planar directions under an NPT ensemble

(constant number of particles, constant pressure, and constant temperature). A temperature of 10 K is considered to limit the influence from temperature fluctuations. The temperature and pressure are maintained by the Nosé–Hoover thermostat and barostat method with a damping time of 0.1 and 1 ps, respectively. Initial velocities of carbon atoms in the systems are assigned following the Gaussian distribution at the given temperature.

To study the tensile mechanical properties of graphene allotrope sheets, the tensile loading along the two directions is simulated by a technology of deformation control under NPT ensembles. It is noted that, as shown in Figure 1, for the pentagraphene and T-graphene, mechanical loads are along the x and xy directions. For other graphene allotropes, mechanical loads are along the x and y directions. A suitable strain rate of 1.0×10^8/s is chosen in the loading simulations. The increment in strain is applied to the structures every 1000 timesteps. The monolayered structures allow the expansion/contraction in a planar direction that is perpendicular to the loading direction during the uniaxial deformation under the NPT ensemble. The atomic stress per atom is calculated based on the virial definition of stress, using the forces on the atoms collected during the MD simulations.[9,10,41] Atomic potential energy and atomic stress are averaged over 1000 timesteps to limit the oscillations.

For the structural characterization of these stretched sheets, detailed microstructure features are examined to identify the structural transformation by exact geometric methods. Using the "shortest path ring" algorithm developed by Franzblau,[42] all of the carbon rings in the modeled structures assuming minimum and maximum carbon-bonding distances of 1.2 and 1.9 Å, respectively, are identified. In our calculations, various carbon rings ranging from trigonal to decagonal motifs are specifically recognized and counted during the tensile process.

ASSOCIATED CONTENT

ⓢ Supporting Information

The Supporting Information is available free of charge on the ACS Publications website at DOI: 10.1021/acsomega.7b00732.

> Bond characteristics of eight graphene allotropes under uniaxial tension loading; development of atomic shear strain in pentagraphene subjected to uniaxial tensions; comparison of the maximum ratio of bond length and bond angle between graphene allotropes; comparison of distribution of atomic von Mises stress in frustrated pentagraphene between x- and xy-directional tensions; comparison of the surface morphology of frustrated pentagraphene between x- and xy-directional tensions; development of polygonal rings in six graphene allotropes under x- and y-directional tensions; and fracture patterns and development of atomic shear strain in graphene allotropes subjected to uniaxial tensions (PDF)

AUTHOR INFORMATION

Corresponding Authors

*E-mail: jianying.he@ntnu.no (J.Y.H.).
*E-mail: chaowang@hit.edu.cn (C.W.).
*E-mail: jianyang@xmu.edu.cn (J.Y.W.).

ORCID ⓘ

Jianying He: 0000-0001-8485-7893
Chao Wang: 0000-0002-1816-5749

Author Contributions

||C.S. and Y.S. contributed equally to this work.

Notes

The authors declare no competing financial interest.

REFERENCES

(1) Howard, J. B.; McKinnon, J. T. Fullerenes C_{60} and C_{70} in Flames. *Nature* **1991**, *352*, 139.

(2) Cataldo, F. From dicopper acetylide to carbyne. *Polym. Int.* **1999**, *48*, 15−22.

(3) Iijima, S. Helical microtubules of graphitic carbon. *Nature* **1991**, *354*, 56.

(4) Novoselov, K. S.; Geim, A. K.; Morozov, S. V.; Jiang, D.; Zhang, Y.; Dubonos, S. V.; Grigorieva, I. V.; Firsov, A. A. Electric field effect in atomically thin carbon films. *Science* **2004**, *306*, 666−669.

(5) Amelinckx, S.; Zhang, X. B.; Bernaerts, D.; Zhang, X. F.; Ivanov, V.; Nagy, J. B. A formation mechanism for catalytically grown helix-shaped graphite nanotubes. *Science* **1994**, *265*, 635.

(6) Artyukhov, V. I.; Liu, M.; Yakobson, B. I. Mechanically induced metal−insulator transition in carbyne. *Nano Lett.* **2014**, *14*, 4224−4229.

(7) Zhang, Y.; Tan, Y.-W.; Stormer, H. L.; Kim, P. Experimental observation of the quantum Hall effect and Berry's phase in graphene. *Nature* **2005**, *438*, 201−204.

(8) Geim, A. K.; Novoselov, K. S. The rise of graphene. *Nat. Mater.* **2007**, *6*, 183−191.

(9) Wu, J.; Nagao, S.; He, J.; Zhang, Z. Nanohinge-induced plasticity of helical carbon nanotubes. *Small* **2013**, *9*, 3561−3566.

(10) Wu, J.; He, J.; Odegard, G. M.; Nagao, S.; Zheng, Q.; Zhang, Z. Giant stretchability and reversibility of tightly wound helical carbon nanotubes. *J. Am. Chem. Soc.* **2013**, *135*, 13775−13785.

(11) Wang, B.-C.; Wang, H.-W.; Chang, J.-C.; Tso, H.-C.; Chou, Y.-M. More spherical large fullerenes and multi-layer fullerene cages. *J. Mol. Struct.: THEOCHEM* **2001**, *540*, 171−176.

(12) Terrones, H.; Terrones, M.; Hernández, E.; Grobert, N.; Charlier, J.-C.; Ajayan, P. M. New metallic allotropes of planar and tubular carbon. *Phys. Rev. Lett.* **2000**, *84*, 1716.

(13) Wang, Z.; Zhou, X.-F.; Zhang, X.; Zhu, Q.; Dong, H.; Zhao, M.; Oganov, A. R. Phagraphene: a low-energy graphene allotrope composed of 5−6−7 carbon rings with distorted Dirac cones. *Nano Lett.* **2015**, *15*, 6182−6186.

(14) Sharma, B. R.; Manjanath, A.; Singh, A. K. Pentahexoctite: a new two-dimensional allotrope of carbon. *Sci. Rep.* **2014**, *4*, 7164.

(15) Mandal, B.; Sarkar, S.; Pramanik, A.; Sarkar, P. Theoretical prediction of a new two-dimensional carbon allotrope and NDR behaviour of its one-dimensional derivatives. *Phys. Chem. Chem. Phys.* **2013**, *15*, 21001−21006.

(16) Liu, Y.; Wang, G.; Huang, Q.; Guo, L.; Chen, X. Structural and electronic properties of T graphene: a two-dimensional carbon allotrope with tetrarings. *Phys. Rev. Lett.* **2012**, *108*, 225505.

(17) Xu, L.-C.; Wang, R.-Z.; Miao, M.-S.; Wei, X.-L.; Chen, Y.-P.; Yan, H.; Lau, W.-M.; Liu, L.-M.; Ma, Y.-M. Two dimensional Dirac carbon allotropes from graphene. *Nanoscale* **2014**, *6*, 1113−1118.

(18) Zhang, S.; Zhou, J.; Wang, Q.; Chen, X.; Kawazoe, Y.; Jena, P. Penta-graphene: a new carbon allotrope. *Proc. Natl. Acad. Sci. U.S.A.* **2015**, *112*, 2372−2377.

(19) Yu, Z. G.; Zhang, Y.-W. A comparative density functional study on electrical properties of layered penta-graphene. *J. Appl. Phys.* **2015**, *118*, 165706.

(20) Cranford, S. W. When is 6 less than 5? Penta- to hexa-graphene transition. *Carbon* **2016**, *96*, 421−428.

(21) Sun, H.; Mukherjee, S.; Singh, C. V. Mechanical properties of monolayer penta-graphene and phagraphene: a first-principles study. *Phys. Chem. Chem. Phys.* **2016**, *18*, 26736−26742.

(22) Fthenakis, Z. G.; Lathiotakis, N. N. Graphene allotropes under extreme uniaxial strain: an ab initio theoretical study. *Phys. Chem. Chem. Phys.* **2015**, *17*, 16418−16427.

(23) Sheng, X.-L.; Cui, H.-J.; Ye, F.; Yan, Q.-B.; Zheng, Q.-R.; Su, G. Octagraphene as a versatile carbon atomic sheet for novel nanotubes, unconventional fullerenes, and hydrogen storage. *J. Appl. Phys.* **2012**, *112*, 074315.

(24) Sun, H.; Mukherjee, S.; Daly, M.; Krishnan, A.; Karigerasi, M. H.; Singh, C. V. New insights into the structure-nonlinear mechanical property relations for graphene allotropes. *Carbon* **2016**, *110*, 443−457.

(25) Zhang, Y.; Pei, Q.; Sha, Z.; Zhang, Y.; Gao, H. Remarkable enhancement in failure stress and strain of penta-graphene via chemical functionalization. *Nano Res.* **2017**, *10*, 1−10.

(26) Le, M.-Q. Mechanical properties of penta-graphene, hydrogenated penta-graphene, and penta-CN 2 sheets. *Comput. Mater. Sci.* **2017**, *136*, 181−190.

(27) Kurokawa, S.; Yamamoto, D.; Hirashige, K.; Sakai, A. Possible formation of one-dimensional chains of C_{20} fullerenes observed by scanning tunneling microscopy. *Appl. Phys. Express* **2016**, *9*, 045102.

(28) Kastner, J.; Kuzmany, H.; Kavan, L.; Dousek, F. P.; Kuerti, J. Reductive preparation of carbyne with high yield. An in situ Raman scattering study. *Macromolecules* **1995**, *28*, 344−353.

(29) Warner, J. H.; Lee, G.-D.; He, K.; Robertson, A. W.; Yoon, E.; Kirkland, A. I. Bond length and charge density variations within extended arm chair defects in graphene. *ACS Nano* **2013**, *7*, 9860−9866.

(30) Kim, B. G.; Jo, J. Y.; Sim, H. S. Comment on "Structural and electronic properties of t graphene: a two-dimensional carbon allotrope with tetrarings". *Phys. Rev. Lett.* **2013**, *110*, 029601.

(31) Neek-Amal, M.; Peeters, F. M. Lattice thermal properties of graphane: thermal contraction, roughness, and heat capacity. *Phys. Rev. B: Condens. Matter Mater. Phys.* **2011**, *83*, 235437.

(32) Qin, Z.; Taylor, M.; Hwang, M.; Bertoldi, K.; Buehler, M. J. Effect of wrinkles on the surface area of graphene: toward the design of nanoelectronics. *Nano Lett.* **2014**, *14*, 6520−6525.

(33) Zhang, T.; Li, X.; Kadkhodaei, S.; Gao, H. Flaw insensitive fracture in nanocrystalline graphene. *Nano Lett.* **2012**, *12*, 4605−4610.

(34) Li, X.; Zhang, S.; Wang, F. Q.; Guo, Y.; Liu, J.; Wang, Q. Tuning the electronic and mechanical properties of penta-graphene via hydrogenation and fluorination. *Phys. Chem. Chem. Phys.* **2016**, *18*, 14191−14197.

(35) Zhou, J.; Wang, Q.; Sun, Q.; Chen, X. S.; Kawazoe, Y.; Jena, P. Ferromagnetism in semihydrogenated graphene sheet. *Nano Lett.* **2009**, *9*, 3867−3870.

(36) Ewels, C. P.; Rocquefelte, X.; Kroto, H. W.; Rayson, M. J.; Briddon, P. R.; Heggie, M. I. Predicting experimentally stable allotropes: Instability of penta-graphene. *Proc. Natl. Acad. Sci. U.S.A.* **2015**, *112*, 15609−15612.

(37) Plimpton, S. Fast parallel algorithms for short-range molecular dynamics. *J. Comput. Phys.* **1995**, *117*, 1−19.

(38) Senftle, T. P.; Hong, S.; Islam, M. M.; Kylasa, S. B.; Zheng, Y.; Shin, Y. K.; Junkermeier, C.; Engel-Herbert, R.; Janik, M. J.; Aktulga, H. M.; Verstraelen, T.; Grama, A.; van Duin, A. C T. The ReaxFF reactive force-field: development, applications and future directions. *npj Comput. Mater.* **2016**, *2*, 15011.

(39) Chenoweth, K.; van Duin, A. C. T.; Goddard, W. A. ReaxFF reactive force field for molecular dynamics simulations of hydrocarbon oxidation. *J. Phys. Chem. A* **2008**, *112*, 1040−1053.

(40) Xu, W.; Zhang, G.; Li, B. Thermal conductivity of penta-graphene from molecular dynamics study. *J. Chem. Phys.* **2015**, *143*, 154703.

(41) Wang, C.; Peng, Q.; Wu, J.; He, X.; Tong, L.; Luo, Q.; Li, J.; Moody, S.; Liu, H.; Wang, R.; Du, S.; Li, Y. Mechanical characteristics of individual multi-layer graphene-oxide sheets under direct tensile loading. *Carbon* **2014**, *80*, 279−289.

(42) Franzblau, D. S. Computation of ring statistics for network models of solids. *Phys. Rev. B: Condens. Matter Mater. Phys.* **1991**, *44*, 4925.